Spin-polarized hybrid states in epitaxially-aligned and rotated graphene on cobalt

Matteo Jugovac[a,c,*], Edward Danquah Donkor[b], Paolo Moras[c], Iulia Cojocariu[a,d], Francesca Genuzio[a], Giovanni Zamborlini[d,1], Giovanni Di Santo[a], Luca Petaccia[a], Nataša Stojić[b], Vitaliy Feyer[d,e], Claus Michael Schneider[d,e], Andrea Locatelli[a], Tevfik Onur Menteş[a,*]

[a] *Elettra - Sincrotrone Trieste, S.S. 14 km 163.5, Basovizza, 34149 Trieste, Italy*
[b] *Abdus Salam International Centre for Theoretical Physics, 34151 Trieste, Italy*
[c] *Istituto di Struttura della Materia-CNR (ISM-CNR), 34149 Trieste, Italy*
[d] *Peter Grünberg Institute (PGI-6), Forschungszentrum Jülich GmbH, 52425 Jülich, Germany*
[e] *Fakultät f. Physik and Center for Nanointegration Duisburg-Essen (CENIDE), Universität Duisburg-Essen, 47048 Duisburg, Germany*

Abstract

The strong interaction between graphene and elemental ferromagnetic transition metals results in considerable shifts of the graphene π band away from the Fermi level. At the same time, a weakly-dispersing single-spin conical band feature is found in the proximity of the Fermi level at the $\overline{\mathrm{K}}$ point in the surface Brillouin zone of epitaxially-aligned graphene/Co(0001). Here, the robustness of this electronic state against twisting angles at the interface is experimentally and theoretically demonstrated by showing the presence of similar band features also in the case of rotated graphene domains on Co(0001). Spin-resolved reciprocal space maps show that the band feature in rotated graphene has similar Fermi velocity and spin polarization as its counterpart in epitaxially-aligned graphene. Density-functional-theory simulations carried out for the experimentally observed graphene orientations, reproduce the highly spin-polarized conical band feature at the graphene $\overline{\mathrm{K}}$ point, characterized by a hybrid π-d orbital character. The presence of the conical features in the rotated domains is attributed to the unfolding of the superstructure $\overline{\mathrm{K}}$ point states exclusively to the $\overline{\mathrm{K}}$ point of the graphene primitive cell. The similarities found in the electronic character for different graphene orientations are crucial in understanding the magnetic properties of realistic graphene/Co interfaces, facilitating the implementation in spintronics applications.

1. Introduction

Owing intrinsically high carrier mobility, small spin-orbit coupling, gate tunability and large spin diffusion length at room temperature, graphene is an ideal candidate for

*Corresponding author
Email addresses: matteo.jugovac@elettra.eu (Matteo Jugovac), tevfik.mentes@elettra.eu (Tevfik Onur Menteş)
[1] Present address: Technische Universität Dortmund, Experimentelle Physik VI, 44227 Dortmund, Germany

the realization of novel, highly efficient spintronic devices [1, 2, 3, 4]. Towards this goal, spin polarization in graphene has been induced by doping, controlling defects and, most effectively, by coupling it to a ferromagnetic material [5, 6, 7, 8, 9, 10]. Among ferromagnetic support materials for graphene, cobalt and nickel have attracted the greatest attention due to the structural matching and the electronic interaction at the interface. In particular, contacting graphene with cobalt was shown to result in a range of phenomena spanning from efficient spin injection [11], spin reorientation in thin cobalt films [12] and the presence of a Rashba-type Dzyaloshinskii-Moriya interaction (DMI) at the graphene-cobalt interface [13, 14, 15]. Notably, the well-known electronic structure of freestanding graphene is remarkably modified due to the strong substrate interaction with graphene π band lying considerably below the Fermi level [16]. Therefore, the basis of spin-related phenomena can rather be attributed to the orbital hybridization at the interface, which results in a spin polarized state near the Fermi level, termed as *minicone* by Usachov *et al.* [17].

Based on the good structural matching between cobalt and graphene [18], most studies on the electronic structure of the graphene-cobalt interface have considered azimuthally-aligned lattices. Indeed, the minicone state has been demonstrated only in the case of graphene lattice aligned with the Ni and Co substrate lattices. Nonetheless, enhanced perpendicular magnetic anisotropy in cobalt is reported also for graphene/Co layers with complete azimuthal disorder [19]. Moreover, there is a range of possible commensurate structures with different azimuthal orientations between two nearly-matching hexagonal layers [20]. Indeed, chemical vapor deposition (CVD) growth of graphene on ultrathin Co films results in rotational disorder at the relatively low growth temperatures necessary to avoid film dewetting [21, 22, 23]. Considering all the research and applications centered around ultrathin films, it is important to understand the effect of rotational disorder by considering both structural and electronic aspects. Thus, we address here the existence of spin polarized minicone bands near the Fermi level in graphene with different rotational alignment with respect to the Co substrate.

In order to investigate the nature of the minicone state depending on the relative in-plane orientation between graphene and cobalt, we use CVD growth with ethylene as the precursor. The growth conditions are adjusted so that graphene domains with symmetry axe aligned or rotated with respect to those of the substrate form. By using spin- and energy-resolved two-dimensional (2D) momentum mapping, we show the presence of very similar electronic states near the Fermi level with linear band dispersion and high degree of spin polarization for both epitaxially-aligned and rotated graphene domains. The experimentally-observed properties of the minicone states are confirmed by density-functional theory (DFT) calculations taking into account the three most abundant graphene rotations at 19.2°, 22.4° and 16.5°. The theoretical calculations indicate that the $\overline{\mathrm{K}}$ points of commensurate Gr/Co superstructures coincide with that of the graphene primitive cell. Furthermore, DFT reveals a high degree of carbon character in the hybridized minicone states for all graphene rotations considered.

2. Methods

2.1. Surface Microscopy and Electron Diffraction

Spectroscopic PhotoEmission and Low-Energy Electron Microscope (SPELEEM, Elmitec) operating at the Nanospectroscopy beamline (Elettra synchrotron, Trieste) [24] was used

for surface microscopy, microspot diffraction and spectroscopy measurements. In the SPELEEM setup, the sample is either illuminated with low-energy electrons (LEEM) or soft X-rays (XPEEM), giving structural and chemical information, respectively [25, 26]. In LEEM, elastically backscattered electrons are directly imaged on a 2D detector through a system of electromagnetic lenses. The electron kinetic energy of the backscattered electrons is selected by tuning a voltage bias applied to the sample (start voltage, V_{st}). In addition to real space imaging, low-energy electron diffraction (LEED) patterns can be collected by imaging the backfocal plane of the objective lens. In diffraction mode operation, the probed area is limited to a micron sized region (μ-LEED) by using an area-selecting aperture. The lateral resolution in real space imaging is better than 10 nm in LEEM and 30 nm in XPEEM, whereas the transfer width in diffraction mode is below 0.05 $Å^{-1}$ [27].

2.2. Spin and Angle Resolved Photoemission Spectroscopy

Spin-resolved ARPES measurements were carried out using the NanoESCA photoemission microscope (PEEM) operating as a branchline at the Nanospectroscopy beamline. In the NanoESCA setup, the sample is illuminated with soft X-rays from the beamline equipped with two Apple-II type undulators. Photon energies cover a range from 40 eV to 1000 eV, and photon polarization can be set to linear horizontal, linear vertical or elliptical. The microscope, by properly tuning the electrostatic lenses, can operate in real space or reciprocal space mode (k-PEEM). The kinetic energy of the photoelectrons is selected by applying a proper bias voltage to the sample, similarly to the SPELEEM instrument. The photoemitted electrons are collected by an optical column, energy filtered in the double-hemispherical configuration (IDEA) and finally projected onto a 2D detector. In addition, spin-dependent reflectivity of a W(001) target inserted in the optical column allows to perform real or reciprocal space imaging with spin resolution. The quantification of the spin polarization can be performed by considering constant the spin sensitivity, being 0.42 and 0.05 for the two employed scattering energies [28]. Therefore the spin polarization P can be given in an interval ranging from -100% (fully spin-down) and +100% (fully spin-up). Prior to spin-resolved measurements the sample was *in-situ* magnetized using a magnetic field of about 0.5 T, sufficient to align the Co magnetic domains along the easy magnetization axis of the W(110) crystal [29, 30].

The high resolution ARPES measurements were carried out at the BaDElPh beamline (Elettra synchrotron, Trieste), using photon energy of 33 eV, s-polarization [31].

2.3. Sample preparation

The W(110) crystal was cleaned by repeated annealing cycles to 1370 K in 3×10^{-7} mbar of molecular oxygen, followed by high temperature flashes in UHV up to 2000°C, until a sharp (1×1) LEED pattern was obtained. The temperature was measured using a C-type thermocouple in the SPELEEM and Bad Elph, and a K-type thermocouple in the NanoESCA setup. Cobalt was deposited using an e-beam evaporator, from a 99.995% purity Co rod, while keeping the sample at room temperature. A total of 50 ML Co was deposited at a rate of 2.3 Å/min. The evaporation rate was determined from the completion of the pseudomorphic bcc(110) layer on W(110) [32], which can be monitored in real-time using LEEM during the growth of the Co adlayer. After

deposition, the quality of the structure and cleanliness of the film was verified by LEED and XPS, respectively. The carbon for the graphene growth was provided by exposing the surface to ethylene (C_2H_4) partial pressure of 5×10^{-7} mbar. The realignment of rotated graphene was performed by annealing the sample under UHV conditions up to 900 K. In all the experiments the base pressure of the preparation and analysis chambers was below 2×10^{-10} mbar.

2.4. Theory

DFT calculations were performed in the plane-wave-pseudopotential approach, as implemented in the PWscf code, a part of the Quantum ESPRESSO distribution [33]. The generalized-gradient approximation for exchange and correlation in the Perdew–Burke–Ernzerhof parametrization and ultrasoft pseudopotentials are used. To account for van der Waals interactions, we applied the empirical DFT-D method [34]. The graphene-covered Co(0001) surfaces are simulated using the supercell method. The computational load due to the large lateral sizes of the rotated phases limited the thickness of the cobalt slab to three layers on top of which was an additional layer of graphene and a vacuum slab equivalent to 7 hexagonal-close packed (hcp) interlayer spacings. Our optimized bulk Co lattice constant is 2.501 Å with c/a ratio of 1.611, which is less than 0.7% smaller than the experimental values of 2.507 Å and c/a of 1.623[35]. For the epitaxially-aligned configuration, we used the fcc-top adsorption geometry [23]. The atomic positions are relaxed in the graphene and the interface Co layer, while the atomic positions in the bottom two Co layers are kept fixed at the bulk values. The $R22°$ phase which we simulated in our calculations can be denoted as $(\sqrt{7}\times\sqrt{7})R40.9°$ supercell. The primitive vectors spanning the unit cell of $R22°$ are rotated by 40.9° with respect to the Co $(10\bar{1}0)$-direction and the graphene is rotated by 21.7° relative to the Co $(10\bar{1}0)$-direction (and the epitaxial alignment) in $R22°$. In the $R19°$ phase, or $(8\times8)R40.9°$ supercell, the graphene is rotated by 19.1° with respect to the Co $(10\bar{1}0)$-direction. Finally, in the $R16°$ phase, denoted as $(7\times7)R36.6°$, graphene is rotated by 16.4° relative to the Co $(10\bar{1}0)$-direction.

3. Results and discussion

Graphene was grown by ethylene CVD on a 50 ML (about 10 nm) Co film on W(110) [36]. Growth at $p_{C2H4} = 5\times10^{-7}$ mbar and $T = 850$ K leads to the formation of various rotational domains of graphene consistently with the literature [21, 23, 37] (further details on sample growth and characterization can be found in the Methods section and in Supporting Material Section 1). Angle resolved photoemission and low-energy electron diffraction (LEED) patterns from the resulting surface featuring both rotated and epitaxially-aligned graphene domains are shown in Figure 1a and 1b, respectively. In the 2D photoelectron momentum map in Figure 1a obtained from the angle resolved photoemission spectroscopy (ARPES) measurement at constant binding energy near the Fermi level, the minicone feature reported in the literature can be discerned at the $\overline{\mathrm{K}}$ point of the epitaxially-aligned graphene domain (green arrow). In addition, a similar band feature is visible also at the respective $\overline{\mathrm{K}}$ points of the rotated graphene domains, as indicated by the red arrows. Based on this observation, we have studied the structural and electronic properties of different graphene domains in a comparative manner.

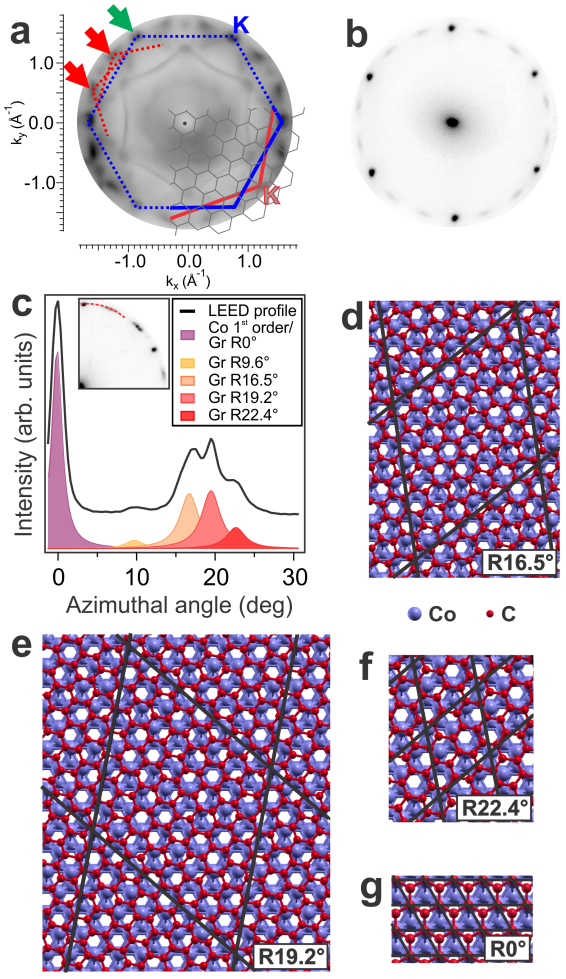

Figure 1: a) 2D momentum map near the Fermi level ($E_b = 50$ meV, $h\nu = 56$ eV, p-polarisation, $T = 130$ K) of coexisting graphene domains with different azimuthal orientations, and b) the corresponding LEED pattern ($V_{st} = 40$ V). Brillouin zones of the cobalt substrate (blue), 19.2° rotated graphene primitive cell (red) and the corresponding Gr/Co superstructure (gray) are shown as an overlay on the bottom right. c) LEED intensity profile acquired along the curved path indicated in the inset. The intensity profile was fitted using Gaussian profiles. Optimized unit-cell geometries from DFT calculations for graphene orientations: d) R19.2°, e) R16.5°, f) R22.4°, g) epitaxially-aligned phase. The black lines denote the surface unit cell, while the red and blue circles represent the C and Co atoms, respectively, in (d-g).

Table 1: The cohesive energy (ΔE in eV per Co surface atom) relative to the epitaxially-aligned case, average distance between the Co surface and graphene ($\overline{d}$ in Å), and isotropic strain of graphene (ϵ in %) are shown for different rotational phases of graphene on Co(0001), based on our DFT calculations.

	R19.2°	R16.8°	R22.4°	R0°
ΔE	0.127	0.127	0.119	0.0
$\overline{d}$	2.13	2.12	2.10	2.08
ϵ	0.61	1.42	1.42	1.42

From the structural perspective, graphene azimuthal orientations and their relative abundance can be quantitatively obtained by measuring the intensity profile in the LEED pattern as seen in Figure 1c along the path indicated in the inset [38]. The azimuthal angle corresponding to the Co(0001) crystal vector is taken as the origin of the angular scale ϕ. By definition, epitaxially-aligned graphene domains appear at $\phi = 0$ (R°). The intensity profile reveals the presence of four broad diffraction peaks rather than a featureless diffraction ring expected from an entirely incoherent azimuthal distribution. The rotations are determined to be $\phi = 9.6°$, 16.5°, 19.2°, 22.4° by fitting the intensity profile with Gaussian peaks. The relative abundance of the $\phi \neq 0$ peaks are 4.7%, 38.2%, 40.6%, 16.5%, respectively. As it can be expected, these angles are close to some of the commensurate orientations found for two matching hexagonal lattices [20], with small differences due to the strain between graphene and the cobalt support.

DFT calculations give further insight into the structural properties of the graphene/Co interface. We consider the three most represented rotated phases, in descending order of abundance: R19.2°, R16.5°, and R22.4° (from here on, the experimentally determined rotation angle will be used to label the respective graphene domain), and compare their structural, energetic and electronic-structure properties to the ones of the epitaxially aligned graphene. The fully relaxed surface unit cell geometries are shown in Figs. 1d-g. The cohesive energy differences between the rotational phases and the epitaxially-aligned one are calculated to be all of the order of 100 meV per Co surface atom as can be seen in Table 1. Furthermore, the average graphene-Co distance, calculated as the difference between the average vertical position of C atoms and the average vertical position of top-layer Co atoms, is larger in the rotational phases as compared to the epitaxially-aligned one by 0.02-0.05 Å. The variations in the C positions for all graphene/Co phases are within 0.05 Å, which is significantly smaller than the typical buckling in graphene Moiré structures such as on Ru(0001) with about 1.5 Å buckling [39]. As for the isotropic tensile strain, R16.5° and R22.4° have the same value as in the epitaxially-aligned phase, while the strain is somewhat smaller in R19.2° (see Table 1).

The computed adsorption geometries consider rotational domains with almost fully relaxed graphene lattices. This is verified experimentally by LEED. The distance between the (00) and the first-order diffraction spots in $\phi \neq 0$ domains is $1.0 \pm 0.4\%$ larger with respect to that of $\phi = 0$ domains, consistently with the rotated domains relaxing towards the lattice constant of freestanding graphene.

Electronic structures of the coexisting epitaxially-aligned and rotated graphene domains are compared in Figure 2. Figure 2a displays the energy-momentum map taken along the $\overline{\mathrm{K\Gamma K}}$ direction of Co(0001), which coincides with the $\overline{\mathrm{K\Gamma K'}}$ direction of the epitaxially-aligned graphene domains. The minicone state is seen at large momenta

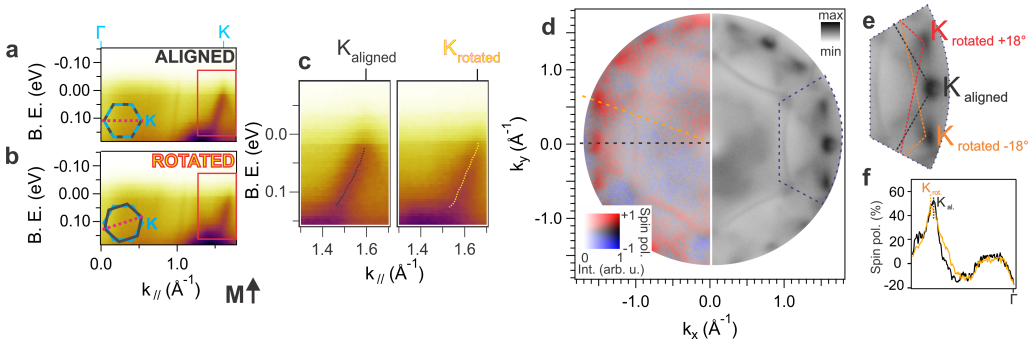

Figure 2: a) Energy-dependent ARPES intensity profile of epitaxially-aligned graphene acquired along the Co $\overline{\mathrm{K\Gamma K}}$ direction near Fermi level. b) Energy-dependent ARPES intensity profile of rotated graphene acquired at 18° with respect to the Co $\overline{\mathrm{K\Gamma K}}$ direction. c) Comparison of the minicone bands for epitaxially-aligned and rotated graphene near their respective $\overline{\mathrm{K}}$ points, with the superimposed linearly dispersed MDC fitted maxima positions. d) Left: 2D spin resolved momentum map (E_B = 90 meV) of the sample composed by both epitaxially-aligned and rotated graphene domains; right: the corresponding spin integrated map. Zoom-in of the dashed region is shown in e). Dashed black, red and orange lines indicate the SBZs of the epitaxially-aligned, +18° and -18° rotated graphene, respectively. f) Spin polarization profile of aligned and rotated graphene acquired along the dashed paths in d)-left. Prior to measurements, the sample was magnetized as shown on bottom of b) panel. All measurements were done at T_s = 130 K using $h\nu$ = 56 eV with p-polarization.

as an intense band with linear dispersion near E_F. The high intensity below about 0.15 eV binding energy corresponds to the Co *3d* states. Instead, Figure 2b shows the energy-momentum map taken at an angle $\phi = 18°$ with respect to the $\overline{\mathrm{K\Gamma K}}$ direction of the Co(0001) substrate. Note that this angle corresponds to the weighted average of coexisting graphene rotational domains as found from the data displayed in Figure 1c. We observe a pattern similar to the epitaxial orientation, characterized by a linearly-dispersive band with the maximum at about 1.7 $\mathrm{Å}^{-1}$ away from $\overline{\Gamma}$ along the $k_{\|}$ direction. The maximum of the minicone state intersects the Fermi level at a slightly larger in-plane momentum transfer with respect to the epitaxially-aligned case (1.74 $\mathrm{Å}^{-1}$ *vs.* 1.70 $\mathrm{Å}^{-1}$, respectively), as better appreciable in Figure 2c. This is consistent with the structural relaxation of the rotated graphene domains observed in LEED. Note that the Co *3d* states appear with similar intensity in both the epitaxially-aligned and rotated profiles.

In order to determine the energy position of the minicone band apex in the case of rotated graphene we measured it with a high-resolution ARPES setup using s-polarized VUV photons as excitation source (see Supporting Information Figure S4). By fitting the momentum map near the Fermi level of rotated graphene acquired along its $\overline{\mathrm{\Gamma K}}$ direction (see Supporting Information Figure S4), the apex of the minicone band is found at a binding energy of 25±15 meV, which is the same as that of epitaxially-aligned graphene. The lateral extent of the surface Brillouin zone (SBZ) is 1.9% larger in the case of rotated graphene with respect to the epitaxially-aligned case, in agreement with the LEED data. Moreover, the rotated minicone bands are broader in $\mathrm{k}_{//}$ than their epitaxially-aligned counterpart, likely due to the presence of domains with slightly varying rotations all contributing to the same band feature. This augmented broadening can be observed in a 2D momentum map acquired close to the Fermi level (E_B = 90 meV), while the minicone bands from epitaxially-aligned graphene have a clear triangular shape (Figure 2d), the

minicone bands from rotated domains appear as elongated bands, aligned perpendicularly to the $\overline{\Gamma K}$ direction of Co(0001).

The Fermi velocity, derived from a linear fit to the measured energy dispersion of the minicone band, is found to be $v_F = 1.66 \times 10^5$ m/s for the epitaxially-aligned phase. In the case of rotated graphene, the corresponding value is $v_F = 1.95 \times 10^5$ m/s, which corresponds to an average over the rotated domains. On the other hand, the π band (main Dirac cone) apex of the rotated phase is found at 2.45 eV with a band velocity of 0.95×10^6 m/s. Therefore, the rotated π band apex is shifted 0.38 eV towards lower binding energies in comparison to epitaxially-aligned graphene [16, 40, 41]. This is in line with a weaker graphene-cobalt interaction in the rotated graphene phase similarly to what has been observed in rotated graphene on Ni(111) [42].

As visible in Figure 2d, upon graphene adsorption, the bands of the Co substrate maintain the same spin behavior as compared to the bare surface (see Supporting Information Figure S5). In particular, minicone bands of epitaxially-aligned domains present a highly spin-polarized majority character (Figure 2d), in line with previously reported results [9, 17, 22, 43, 16]. Using the procedure described in ref. [44, 28], the determined value of the spin polarization on the minicone in the epitaxially-aligned domains corresponds to 53±8%. Importantly, the minicone bands of rotated graphene present the same spin behavior as the epitaxially-aligned one. The measured value of spin polarization in the case of rotated graphene is 47±7%, which is comparable to the value of the epitaxially-aligned one. Note that the measured degree of spin-polarization can be underestimated due to the presence of magnetic domains as the measurement is done in remanence.

The nature and the origin of this linearly-dispersing spin-polarized state near Fermi level can be better understood by DFT calculations. Figure 3 shows the calculated band structures along the $\overline{\Gamma K}$ direction for both majority and minority spins of $R19.2°$, and only majority spin of $R16.5°$, $R22.4°$ and the epitaxially-aligned phase. Each band structure is unfolded from its respective supercell to the 1×1 graphene primitive cell [45]. Each of the phases possesses a minicone-like feature in the spin majority channel at the $\overline{K}$ point. By comparing majority and minority spin channels of $R19.2°$ in Figs. 3a) and b), it can be concluded that in our calculations the minicone is almost fully spin polarized (for the other phases and for the main Dirac cones, see Supporting Information Section 4). Furthermore, the minicones of the rotated-graphene phases have a roughly similar appearance as the minicone of the epitaxially-aligned phase, but with a more pronounced linear dispersion.

The minicone bandgap opening in the rotated phases is of the order of a few meV as can be seen in Figs. 3(a-c), while the corresponding value for epitaxially-aligned graphene is 0.4 eV. In binding energy the minicone apex is found at 0.311 eV for $R19.2°$, 0.259 eV for $R22.4°$ and 0.267 eV for $R16.5°$, while in the epitaxially-aligned phase it is found at 0.302 eV binding energy. All these values are $0.23-0.29$ eV larger compared to the experimental binding energy of the minicone. Similar binding energies of the highest valence states at K have been observed earlier for the DFT band structures of the epitaxially-aligned graphene/Co(0001) in generalized-gradient approximation [46, 47, 43]. While inclusion of van-der-Waals non-local correlation functional with GGA exchange improves overall comparison of the electronic structure with experiment relative to GGA [46], a full consideration of self-energy effects is necessary for further reduction of the quantitative shift of the minicone binding energy between theory and experiment and for better

comparison with the experimental dispersions [48, 49].

Estimated theoretical Fermi velocities of the minicone in the rotated phases at $\overline{\mathrm{K}}$ in the $\overline{\Gamma\mathrm{K}}$ direction vary from 2.3×10^5 m/s (R22.4°) to 2.6×10^5 m/s (R19.2°) and are significantly enhanced with respect to the estimated Fermi velocity of the epitaxially-aligned graphene (1.3×10^5 m/s). The increase of the Fermi velocity can be considered a further indication of a weaker substrate interaction in the rotated phase in comparison to the epitaxially-aligned graphene, as the stronger interactions due to the reduction of the graphene-Co distance are shown to flatten the minicone in the epitaxially-aligned graphene around the $\overline{\mathrm{K}}$ point. Note that the calculated band velocities compare reasonably well with the experimental values, confirming the correspondence between the experimentally-observed band feature and the calculated one.

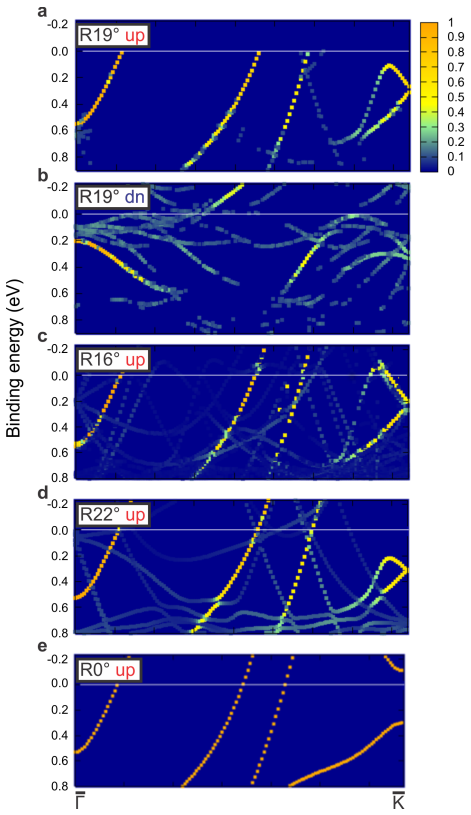

Figure 3: The calculated band structures for different rotated phases of graphene on Co(0001) unfolded into the 1×1 graphene primitive unit cell along $\overline{\Gamma\mathrm{K}}$ direction for a) majority and b) minority spin channels of $R19.2°$; majority spin channels of c) $R16.5°$, d) $R22.4°$ phase; d) the majority spin channel of the epitaxially-aligned graphene. The color bar indicates the strength of the primitive-cell character of the unfolded states. The unfolding has been performed using the BandUP code [45].

Notably, orbital projections indicate a high degree of carbon orbital nature of the mini-cone states at $\overline{\mathrm{K}}$ (see Supporting information Figure S6). In the majority spin channel carbon character of the minicone states in the rotated phases is estimated to be above 40% [50], which is comparable to the calculated value of 55% for the epitaxially-

aligned phase.

Furthermore, we also show the graphene primitive-cell character in Figure 3 in color code, based on the spectral-weight calculation during the unfolding procedure, [45] which gives the probability that the eigenstate in the supercell has the same character as the primitive cell Bloch state to which it unfolds. The primitive character is a measure of the superlattice's modulation of the electronic structure with respect to the primitive cell. The unfolded mini-cone state at $\overline{\mathrm{K}}$ is trivially strongest in the epitaxially-aligned phase since the supercell coincides with the primitive cell. In the rotated phases, the primitive cell character is approximately 60%. In all the rotated phases considered, the states at $\overline{\mathrm{K}}$ of the graphene primitive cell are unfolded exclusively from the $\overline{\mathrm{K}}$ points of the superstructure unit cell. This results in the appearance of the minicones both at the primitive and supercell $\overline{\mathrm{K}}$ points and explains the observation that the minicone appears at the $\overline{\mathrm{K}}$ point of the primitive cell even in the rotated phases (overlay inset in Figure 1a). Finally, the fact that the minicone has a more linear dispersion and is found at lower binding energy in the rotated phases relative to the epitaxially-aligned one is likely related to the specific strength of graphene-Co binding in the rotated phases. In the rotated phases, the binding is weaker than in the epitaxially-aligned phase, but the graphene-Co distances are still in the range of chemisorption distances and graphene appears without any rippling.

4. Conclusion

In this work, we demonstrate experimentally that epitaxially-aligned and rotated graphene domains host highly spin-polarized minicone features at the $\overline{\mathrm{K}}$ points of the respective graphene SBZ. The experimental findings are reproduced by DFT calculations performed for the four prevalent orientations of graphene on Co(0001). The calculations reveal a similar graphene character of the minicones in the rotated phases and the epitaxially-aligned phase. Furthermore, a smaller band-gap opening and a dispersion of the minicone closer to linear in the rotated phases, with respect to the epitaxially-aligned phase, have been found in the calculated band structures. In particular, an enhanced Fermi velocity of the minicone state with respect to the epitaxially-aligned graphene one has been observed both experimentally and theoretically. We find that all our experimental and theoretical findings originate from (i) the fact that the superstructure states at $\overline{\mathrm{K}}$, and thus the minicone states, unfold exclusively to the $\overline{\mathrm{K}}$ states in the primitive cell and (ii) the weaker graphene-Co binding in the rotational phases (due to the loss of C and Co orbital alignment) relative to the epitaxially-aligned phase, but which keeps some characteristics of chemisorbed graphene.

Considering the unavoidable presence of different rotational alignments of graphene grown especially on ultrathin Co films, our findings provide a solid experimental and theoretical basis for exploiting CVD synthesized graphene/Co(0001) interfaces in spintronics. Moreover, the similarities between graphene/Co(0001) and graphene/Ni(111), and to a lesser extent graphene/Fe, indicate that our results can be generalized also to other ferromagnetic substrates.

Acknowledgments

We acknowledge Prof. Sebastian Günther for fruitful discussions.

Appendix A. Supplementary data

Supplementary data related to this article can be found at ...

References

[1] Z. Han, A. Kimouche, D. Kalita, A. Allain, H. Arjmandi-Tash, A. Reserbat-Plantey, L. Marty, S. Pairis, V. Reita, N. Bendiab, J. Coraux, V. Bouchiat, Homogeneous Optical and Electronic Properties of Graphene Due to the Suppression of Multilayer Patches During CVD on Copper Foils, Advanced Functional Materials 24 (2014) 964–970.

[2] A. Soumyanarayanan, N. Reyren, A. Fert, C. Panagopoulos, Emergent phenomena induced by spin–orbit coupling at surfaces and interfaces, Nature 539 (2016) 509–517.

[3] Q. Wu, L. Shen, Z. Bai, M. Zeng, M. Yang, Z. Huang, Y. P. Feng, Efficient spin injection into graphene through a tunnel barrier: Overcoming the spin-conductance mismatch, Phys. Rev. Applied 2 (2014) 044008.

[4] B. Dlubak, M.-B. Martin, C. Deranlot, B. Servet, S. Xavier, R. Mattana, M. Sprinkle, C. Berger, W. A. De Heer, F. Petroff, A. Anane, P. Seneor, A. Fert, Highly efficient spin transport in epitaxial graphene on sic, Nature Physics 8 (2012) 557–561.

[5] T. S. Ghiasi, A. A. Kaverzin, A. H. Dismukes, D. K. de Wal, X. Roy, B. J. van Wees, Electrical and thermal generation of spin currents by magnetic bilayer graphene, Nature Nanotechnology 16 (2021) 788–794.

[6] T. Enoki, K. Takai, The edge state of nanographene and the magnetism of the edge-state spins, Solid State Communications 149 (2009) 1144–1150.

[7] O. V. Yazyev, L. Helm, Defect-induced magnetism in graphene, Physical Review B 75 (2007) 125408.

[8] P. O. Lehtinen, A. S. Foster, Y. Ma, A. V. Krasheninnikov, R. M. Nieminen, Irradiation-induced magnetism in graphite: a density functional study, Physical review letters 93 (2004) 187202.

[9] Y. S. Dedkov, M. Fonin, Electronic and magnetic properties of the graphene–ferromagnet interface, New Journal of Physics 12 (2010) 125004.

[10] R. Decker, J. Brede, N. Atodiresei, V. Caciuc, S. Blügel, R. Wiesendanger, Atomic-scale magnetism of cobalt-intercalated graphene, Phys. Rev. B 87 (2013) 041403.

[11] J. Pan, S. Du, Y. Zhang, L. Pan, Y. Zhang, H.-J. Gao, S. T. Pantelides, Ferromagnetism and perfect spin filtering in transition-metal-doped graphyne nanoribbons, Phys. Rev. B 92 (2015) 205429.

[12] A. D. Vu, J. Coraux, G. Chen, A. T. N'Diaye, A. K. Schmid, N. Rougemaille, Unconventional Magnetisation Texture in Graphene/Cobalt Hybrids, Scientific Reports 6 (2016) 24783.

[13] H. Yang, G. Chen, A. A. C. Cotta, A. T. N'Diaye, S. A. Nikolaev, E. A. Soares, W. A. A. Macedo, K. Liu, A. K. Schmid, A. Fert, et al., Significant Dzyaloshinskii–Moriya interaction at graphene–ferromagnet interfaces due to the Rashba effect, Nature materials 17 (2018) 605.

[14] F. Ajejas, A. Gudin, R. Guerrero, A. Anadón Barcelona, J. M. Diez, L. de Melo Costa, P. Olleros, M. A. Nino, S. Pizzini, J. Vogel, M. Valvidares, P. Gargiani, M. Cabero, M. Varela, J. Camarero, R. Miranda, P. Perna, Unraveling Dzyaloshinskii-Moriya Interaction and Chiral Nature of Graphene/Cobalt Interface, Nano Letters 18 (2018) 5364–5372.

[15] A. Hallal, J. Liang, F. Ibrahim, H. Yang, A. Fert, M. Chshiev, Rashba-type dzyaloshinskii–moriya interaction, perpendicular magnetic anisotropy, and skyrmion states at 2d materials/co interfaces, Nano Letters 21 (2021) 7138–7144.

[16] A. Varykhalov, D. Marchenko, J. Sánchez-Barriga, M. R. Scholz, B. Verberck, B. Trauzettel, T. O. Wehling, C. Carbone, O. Rader, Intact Dirac Cones at Broken Sublattice Symmetry: Photoemission Study of Graphene on Ni and Co, Physical Review X 2 (2012) 041017.

[17] D. Usachov, A. Fedorov, M. M. Otrokov, A. Chikina, O. Vilkov, A. Petukhov, A. G. Rybkin, Y. M. Koroteev, E. V. Chulkov, V. K. Adamchuk, A. Grüneis, C. Laubschat, D. V. Vyalikh, Observation of Single-Spin Dirac Fermions at the Graphene/Ferromagnet Interface, Nano Letters 15 (2015) 2396–2401.

[18] S. Günther, P. Zeller, Moiré Patterns of Graphene on Metals, in: K. Wandelt (Ed.), Encyclopedia of Interfacial Chemistry, Elsevier, Oxford, 2018, pp. 295 – 307.

[19] P. Genoni, F. Genuzio, T. O. Menteş, B. Santos, A. Sala, C. Lenardi, A. Locatelli, Magnetic Patterning by Electron Beam-Assisted Carbon Lithography, ACS Applied Materials & Interfaces 10 (2018) 27178–27187.

[20] A. O. Sboychakov, A. L. Rakhmanov, A. V. Rozhkov, F. Nori, Electronic spectrum of twisted bilayer graphene, Phys. Rev. B 92 (2015) 075402.
[21] H.-C. Mertins, C. Jansing, M. Krivenkov, A. Varykhalov, O. Rader, H. Wahab, H. Timmers, A. Gaupp, A. Sokolov, M. Tesch, P. M. Oppeneer, Giant magneto-optical faraday effect of graphene on co in the soft x-ray range, Phys. Rev. B 98 (2018) 064408.
[22] A. Varykhalov, O. Rader, Graphene Grown on Co(0001) Films and Islands: Electronic Structure and its Precise Magnetization Dependence, Physical Review B 80 (2009) 035437.
[23] M. Jugovac, F. Genuzio, E. L. Gonzalez, N. Stojić, G. Zamborlini, V. Feyer, T. O. Menteş, A. Locatelli, C. M. Schneider, Role of carbon dissolution and recondensation in graphene epitaxial alignment on cobalt, Carbon 152 (2019) 4.
[24] A. Locatelli, L. Aballe, T. O. Mentes, M. Kiskinova, E. Bauer, Photoemission Electron Microscopy with Chemical Sensitivity: SPELEEM Methods and Applications, Surface and Interface Analysis 38 (2006) 1554–1557.
[25] A. Locatelli, E. Bauer, Recent Advances in Chemical and Magnetic Imaging of Surfaces and Interfaces by XPEEM, Journal of Physics: Condensed Matter 20 (2008) 093002.
[26] E. Bauer, Surface Microscopy with Low-Energy Electrons, Springer-Verlag New York, 2014.
[27] T. O. Menteş, G. Zamborlini, A. Sala, A. Locatelli, Cathode Lens Spectromicroscopy: Methodology and Applications, Beilstein Journal of Nanotechnology 5 (2014) 1873–1886.
[28] C. Tusche, M. Ellguth, A. Krasyuk, A. Winkelmann, D. Kutnyakhov, P. Lushchyk, K. Medjanik, G. Schönhense, J. Kirschner, Quantitative spin polarization analysis in photoelectron emission microscopy with an imaging spin filter, Ultramicroscopy 130 (2013) 70–76.
[29] A. P. Bartlett, In-plane anisotropy of ultrathin Co/W(110) films and the Néel transition in bilayer ultrathin CoO/Co/W(110) films, Master thesis at McMaster University (2013).
[30] J. E. Prieto, O. Krupin, S. Gorovikov, K. Döbrich, G. Kaindl, K. Starke, Magnetism of ordered Sm/Co(0001) surface structures, Physical Review B 72 (2005) 092409.
[31] L. Petaccia, P. Vilmercati, S. Gorovikov, M. Barnaba, A. Bianco, D. Cocco, C. Masciovecchio, A. Goldoni, Bad ElPh: A 4m normal-incidence monochromator beamline at Elettra, Nuclear Instruments and Methods in Physics Research Section A: Accelerators, Spectrometers, Detectors and Associated Equipment 606 (2009) 780–784.
[32] H. Knoppe, E. Bauer, Electronic structure of ultrathin cobalt films on w(110), Physical Review B 48 (1993) 1794–1805.
[33] P. Giannozzi, QUANTUM ESPRESSO: a Modular and Open-Source Software Project for Quantum Simulations of Materials, Journal of Physics: Condensed Matter 21 (2009) 395502.
[34] J. Antony, S. Grimme, Density functional theory including dispersion corrections for intermolecular interactions in a large benchmark set of biologically relevant molecules, Physical Chemistry Chemical Physics 8 (2006) 5287–5293.
[35] A. Taylor, R. W. Floyd, Precision Measurements of Lattice Parameters of Non-Cubic Crystals, Acta Crystallographica 3 (1950) 285–289.
[36] M. Jugovac, Morphology and electronic structure of graphene supported by metallic thin films, Dr., Universität Duisburg, Jülich, 2020. Universität Duisburg, Diss., 2020.
[37] H. Ago, Y. Ito, N. Mizuta, K. Yoshida, B. Hu, C. M. Orofeo, M. Tsuji, K. ichi Ikeda, S. Mizuno, Epitaxial Chemical Vapor Deposition Growth of Single-Layer Graphene over Cobalt Film Crystallized on Sapphire., ACS Nano 4 (2010) 7407–7414.
[38] H. Hattab, A. T. N'Diaye, D. Wall, G. Jnawali, J. Coraux, C. Busse, R. van Gastel, B. Poelsema, T. Michely, F.-J. M. zu Heringdorf, M. H. von Hoegen, Growth temperature dependent graphene alignment on Ir(111), Applied Physics Letters 98 (2011) 141903.
[39] B. Wang, M.-L. Bocquet, S. Marchini, S. Günther, J. Wintterlin, Chemical origin of a graphene moiré overlayer on Ru(0001), Phys. Chem. Chem. Phys. 10 (2008) 3530–3534.
[40] M. Jugovac, F. Genuzio, T. O. Menteş, A. Locatelli, G. Zamborlini, V. Feyer, C. M. Schneider, Tunable coupling by means of oxygen intercalation and removal at the strongly interacting graphene/cobalt interface, Carbon 163 (2020) 341–347.
[41] M. Jugovac, C. Tresca, I. Cojocariu, G. Di Santo, W. Zhao, L. Petaccia, P. Moras, G. Profeta, F. Bisti, Clarifying the apparent flattening of the graphene band near the van Hove singularity, Phys. Rev. B 105 (2022) L241107.
[42] C. Africh, C. Cepek, L. L. Patera, G. Zamborlini, P. Genoni, T. O. Menteş, A. Sala, A. Locatelli, G. Comelli, Switchable Graphene-Substrate Coupling Through Formation/Dissolution of an Intercalated Ni-Carbide Layer, Scientific Reports 6 (2016) 19734.
[43] D. Marchenko, A. Varykhalov, J. Sánchez-Barriga, O. Rader, C. Carbone, G. Bihlmayer, Highly spin-polarized Dirac fermions at the graphene/Co interface, Physical Review B 91 (2015) 235431.

[44] C. Tusche, M. Ellguth, A. A. Ünal, C.-T. Chiang, A. Winkelmann, A. Krasyuk, M. Hahn, G. Schönhense, J. Kirschner, Spin resolved photoelectron microscopy using a two-dimensional spin-polarizing electron mirror, Applied Physics Letters 99 (2011) 032505.

[45] P. V. Medeiros, S. Stafström, J. Björk, Effects of extrinsic and intrinsic perturbations on the electronic structure of graphene: Retaining an effective primitive cell band structure by band unfolding, Physical Review B 89 (2014) 041407.

[46] G. M. Sipahi, I. Žutić, N. Atodiresei, R. K. Kawakami, P. Lazić, Spin polarization of Co(0001)/graphene junctions from first principles, Journal of Physics: Condensed Matter 26 (2014) 104204.

[47] E. Voloshina, Y. Dedkov, Electronic and magnetic properties of the graphene- ferromagnet interfaces: Theory vs. experiment, in: S. Mikhailov (Ed.), Physics and Applications of Graphene: Experiments, BoD – Books on Demand, 2011.

[48] A. Grechnev, I. Di Marco, M. I. Katsnelson, A. I. Lichtenstein, J. Wills, O. Eriksson, Theory of bulk and surface quasiparticle spectra for Fe, Co, and Ni, Phys. Rev. B 76 (2007) 035107.

[49] P. E. Trevisanutto, C. Giorgetti, L. Reining, M. Ladisa, V. Olevano, Ab Initio *GW* Many-Body Effects in Graphene, Phys. Rev. Lett. 101 (2008) 226405.

[50] Note:, The calculated C-character in the rotational phases from the projection on the atomic orbitals is likely the lower limit considering that the atomic orbitals on which the projection is done are in the coordinate system defined by the Co atoms (and at angles of e.g. 19°, 16° and 22° with respect to the C-C bonds). This is not the case for the projection on atomic orbitals in the aligned phase.